Probing carrier and phonon transport in semiconductors all at once through frequency-domain photoreflectance

Qichen Song[,1,*] Sorren Warkander[,2] and Samuel C. Huberman[3,†]

[1]*Department of Chemistry and Chemical Biology, Harvard University, Cambridge, Massachusetts 02138, USA*
[2]*Chemical Sciences Division, Lawrence Berkeley National Laboratory, Berkeley, California 94720, USA*
[3]*Department of Chemical Engineering, McGill University, Montreal, Quebec H3A 0C5, Canada*

Semiconductor devices favor high carrier mobility for reduced Joule heating and high thermal conductivity for rapid heat dissipation. The ability to accurately characterize the motion of charge carriers and heat carriers is necessary to improve the performance of electronic devices. However, the conventional approaches of measuring carrier mobility and thermal conductivity require separate and independent measurement techniques. These techniques often involve invasive probing, such as depositing thin metal films on the sample as Ohmic contacts for characterizing electrical transport or as optical transducers for characterizing thermal transport, which becomes more cumbersome as the geometry of the semiconductor devices becomes small and complicated. Here we demonstrate a noncontact frequency-domain pump-probe method that requires no sample pretreatment to simultaneously probe carrier and phonon transport. We find that the optical reflectance depends on both excess carriers and phonons in response to exposure to a modulated continuous-wave pump laser source. By modeling the ambipolar diffusion of photoinduced excess carriers, energy transfer between electrons and phonons, and phonon diffusion, we are able to extract temperature-dependent electrical and thermal transport coefficients in Si, Ge, SiGe, and GaAs. The continuous-wave pump and probe lasers enable a more efficient and compact experimental setup for the assessment of electrical transport than conventional pulsed-laser methods. Our approach provides a convenient and accurate platform for the study of the charge transport and energy dissipation in semiconductors.

I. INTRODUCTION

In the age of artificial intelligence, we witness an ever-growing demand for computation. Modern computer chips consist of semiconductor transistors as the fundamental building block and the transistor density has grown rapidly from several hundreds to over one hundred million per mm^2 during the past half century [1,2]. However, the power density has grown concurrently, leading to the formidable challenge of effectively dissipating the increasing amount of heat [3,4]. To suppress the heat generation and enhance the heat dissipation, materials with high carrier mobility, which causes less Joule heating and high phonon thermal conductivity, which lowers the chip temperature rise are desirable. The ability to accurately characterize the carrier and phonon transport in semiconductor devices is vital for the discovery of materials with desired properties and the rational design of electronic devices with boosted efficiency. Conventionally, carrier transport and phonon transport are separately characterized with different techniques. For instance, the carrier mobility can be measured by the time-of-flight technique [5] or Hall effect measurement [6], and the thermal conductivity can be measured using the 3ω method [7], time-domain thermoreflectance (TDTR) [8–10] or frequency-domain thermoreflectance (FDTR) [11,12]. However, these transport characterization techniques all require the deposition of a metallic film on the sample as an electrode or a heater, which significantly lowers the sensitivity to the transport coefficients in thin-film samples.

Direct optical pump-probe measurement on the bare sample is a truly noninvasive method, at the cost of creating a more complicated coupled transport scenario where the electronic and lattice degrees of freedom are both excited. Transient reflectance over several tens of picoseconds after the pump laser pulse encodes transient carrier density and temperature rise. For example, in silicon, the carrier and temperature contribute to the transient reflectance at 760 nm with opposite signs [13]. The transient grating (TG) technique [14,15] has been used to probe the ambipolar mobility and thermal conductivity

*qichensong@g.harvard.edu
†samuel.huberman@mcgill.ca

simultaneously in cubic boron arsenide, where a pulsed probe and a cw probe are used to probe the carrier ambipolar diffusion at short times (approximately 100 ps) and the phonon transport in the long times (approximately 100 ns), respectively [16,17]. TDTR without using metal transducer [18,19] has recently been used to measure the thermal conductivity in semiconductors and the contribution of the carrier to the signal is modeled and subtracted. However, under a pulsed pump the carrier-induced part of the signal decay rapidly with time. And a substantial number of carriers need to be excited initially, yet they experience complicated high-order recombination processes and strong electron-phonon interactions [20,21], making it difficult to fit the electrical transport properties with enough fidelity. In contrast, conducting the pump-probe measurement in the frequency domain using modulated cw lasers only weakly perturbs the material with an amplitude uniform in time, which is closer to the actual transport regime in devices. Transducerless FDTR using cw lasers has been used to measure several selected materials with minimal carrier effect such that the signal is still proportional to temperature [22,23]. However, the temporal behavior of optical reflectance under modulated laser irradiation encodes information about the dynamics of charge carriers [24] yet the ability to simultaneously probe electrical and thermal transport in frequency-domain photoreflectance measurement has never been explored.

In this paper, we present a method of probing the carrier and phonon transport in semiconductors in the frequency domain, where the time-harmonic responses of carrier and phonon coexist. The difference between the electron temperature and phonon temperature is found to be insignificant below the characteristic frequency for electron-phonon coupling determined by the material properties. The carrier diffusion is nearly in-phase, whereas the phonon diffusion is responsible for a larger phase lag that varies more rapidly with modulation frequency. This difference in the dependence on modulation frequency enables the extraction of the ambipolar diffusion coefficient and phonon thermal conductivity in a single-shot frequency-sweep measurement. Our work provides a simple approach to characterize the carrier and phonon transport in semiconductors, which can be readily applied to the study of actual devices.

II. RESULTS AND DISCUSSION

We use a 458-nm cw pump laser with its power being modulated at the given frequency f. The pump-induced change in reflectance of a 532-nm probe laser is modulated by the relevant excited degrees of freedom in the material at the same frequency such that $\Delta R(t) = \Delta R e^{i\omega t}$, where $\omega = 2\pi f$ is the angular frequency. Because of the optically induced nature, we call ΔR the photoreflectance. More details of the experimental setup can be

found in Sec. III. Figure 1 presents the carrier dynamics in semiconductors under the irradiation of a modulated laser. The absorbed pump photons excite electrons across the band gap to generate electron-hole pairs. The excess electrons/holes then start to diffuse away from the center of the pump laser spot [Fig. 1(b)]. When colliding with other carriers and phonons, the excited electrons/holes quickly thermalize (within 1 ps in silicon [25]) among themselves via electron-electron scattering [26,27] and electron-phonon scattering [28], particularly with phonons that have low energy and high momentum to populate different valleys. The thermalized electrons follow a quasi-Fermi-Dirac distribution with an effective electron temperature T_{el}, referred to as hot-electron temperature [29] and an effective chemical potential $E_{\mathrm{F,c}}$. Accordingly, the number density of excess hot electrons is given by $\rho = \int g_{\mathrm{c}}(E) \left[e^{(E - E_{\mathrm{F,c}})/k_{\mathrm{B}} T_{\mathrm{el}}} + 1 \right]^{-1} dE - \rho_0$, where $g_{\mathrm{c}}(E)$ is the density of states for conduction-band electrons, k_{B} is the Boltzmann constant, and ρ_0 is the number density of free electrons without the pump laser excitation. Similarly, there exist an effective temperature T_{h} and an effective chemical potential $E_{\mathrm{F,v}}$ for the hot holes. For simplicity, we assume that the electron and hole temperatures are the same, represented by a single variable T_{el}, which is a reasonable approximation for common semiconductors [30]. The hot electrons and holes gradually transfer their energy to the lattice via electron-phonon interaction [28], which heats up the phonon subsystem. The phonons thermalize with other phonons through anharmonic phonon-phonon scattering achieving a local temperature T_{ph} and diffuse towards colder areas, depicted in Fig. 1(c). In parallel to these scattering events, the electrons and holes experience frequent recombination events that annihilate electron-hole pairs [Fig. 1(a)].

To quantify the pump-induced dynamics, we model the transport processes of excited charge and energy carriers using the ambipolar diffusion equation with carrier generation and recombination, the electronic heat equation and the phonon heat equation with electron-phonon energy transfer,

$$\frac{\partial \rho}{\partial t} = \nabla \cdot \mathbf{D}_a \cdot \nabla \rho - \frac{\rho}{\tau} + \frac{P}{E_{\mathrm{photon}}}, \quad (1)$$

$$C_{\mathrm{el}} \frac{\partial T_{\mathrm{el}}}{\partial t} = \nabla \cdot \boldsymbol{\kappa}_{\mathrm{el}} \cdot \nabla T_{\mathrm{el}} - g_{\mathrm{e-p}} \left(T_{\mathrm{el}} - T_{\mathrm{ph}} \right)$$

$$+ \frac{\rho E_{\mathrm{gap}}}{\tau} + \frac{P \Delta E}{E_{\mathrm{photon}}}, \quad (2)$$

$$C_{\mathrm{ph}} \frac{\partial T_{\mathrm{ph}}}{\partial t} = \nabla \cdot \boldsymbol{\kappa}_{\mathrm{ph}} \cdot \nabla T_{\mathrm{ph}} + g_{\mathrm{e-p}} \left(T_{\mathrm{el}} - T_{\mathrm{ph}} \right), \quad (3)$$

where ρ, T_{el}, and T_{ph} are the excess carrier density, electron temperature, and phonon temperature, respectively. C_{el} is the total volumetric heat capacity of electrons and
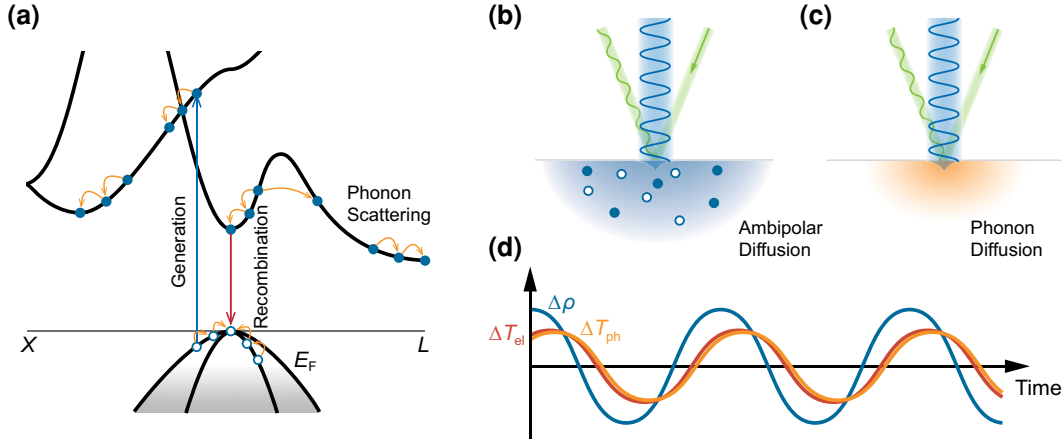
FIG. 1. Schematic for the frequency-domain photoreflectance. (a) The carrier dynamics induced by pump photons in p-type Ge. The incident photon first generates an electron-hole pair across the direct band gap. The excess free carriers (electrons and holes) interact with phonons and quickly thermalize achieving the electron temperature T_{el}. The phonons are excited by those hot carriers and the phonon temperature is T_{ph}. (b),(c) The pump and probe laser geometry in experiment. The reflectance for the probe beam is modulated by the carriers and phonons. The intensity of the reflected probe beam consists of dc and ac parts. The ac part contains the information of transport processes including carrier diffusion (b) and phonon diffusion (c),(d). The real parts of the ac signals due to excess carriers, electron temperature and phonon temperature dynamics. The power of the modulated pump is assumed to be $P(t) \propto e^{i\omega t}$ and its real part is a cosine wave $\mathrm{Re}\{P(t)\} \propto \cos(\omega t)$. In semiconductors with strong electron-phonon interaction under a modest modulation frequency, the electron and phonon temperatures are approximately the same. The carriers normally diffuse faster than phonons, thus having a smaller phase lag.

holes and C_{ph} is the volumetric heat capacity of phonons. $\mathbf{D}_a$, $\boldsymbol{\kappa}_{el}$, and $\boldsymbol{\kappa}_{ph}$ are the ambipolar diffusivity, electronic thermal conductivity [31] and phonon thermal conductivity tensors. g_{e-p} is the electron-phonon coupling factor. τ is the effective lifetime of the excess carrier, predominantly determined by the radiative recombination process caused by above-band-gap photon emission at modest defect concentrations [32]. E_{photon} is the energy of a pump photon. $P = 2P_0\alpha/(\pi\sigma_x\sigma_y)e^{-2x^2/\sigma_x^2}e^{-2y^2/\sigma_y^2}e^{-\alpha z}e^{i\omega t}$ is the absorbed laser power density. Here α is the inverse penetration depth for the pump beam. $P_0 = P_{pump}(1 - R)$ is the absorbed pump power, with P_{pump} the peak pump power, $R = ((n-1)^2 + \kappa^2)/((n+1)^2 + \kappa^2)$ the reflectance at the pump wavelength, and n and κ the real and imaginary parts of the refractive index. σ_x and σ_y are the $1/e^2$ beam radii for the pump beam in x and y directions. E_{gap} is the direct band gap energy and the second-to-last term in Eq. (2) describes the heating due to carrier recombination. The remaining energy transferred from a photon to the hot-carrier ensemble is given by $\Delta E = E_{photon} - E_{gap}$, where the energy-transfer process is considered as instantaneous. We apply the Fourier transform to Eqs. (1)–(3) in the in-plane directions to solve for $\tilde{\rho}(\mathbf{q}_{\parallel}, z, t)$, $\tilde{T}_{el}(\mathbf{q}_{\parallel}, z, t)$ and $\tilde{T}_{ph}(\mathbf{q}_{\parallel}, z, t)$, where $\mathbf{q}_{\parallel}$ is the in-plane reciprocal vector. Then, the inverse Fourier transform renders the spatial profiles of $\rho(\mathbf{r}, t)$, $T_{el}(\mathbf{r}, t)$, and $T_{ph}(\mathbf{r}, t)$ (Secs. II and III within the Supplemental Material [33]). Note that the carrier

density and temperatures are deviations (ac parts) from their corresponding background values rather than the absolute values (dc+ac parts). For conciseness, we will refer to the deviation in the excess carrier density as the excess carrier density and the deviation in temperature as temperature in the following.

The photoreflectance of the probe beam encodes the contributions from the time-varying excess carrier density, electron, and phonon temperatures. In the limit of linear response,

$$\frac{\Delta R}{R} = \mathrm{Re}\left\{A\overline{\rho} + B\overline{T}_{el} + C\overline{T}_{ph}\right\}, \tag{4}$$

where the overline indicates the weighted average of the physical quantity X over the probe beam profile, such that $\overline{X} = 2\gamma/\pi\sigma_x'\sigma_y' \int X(\mathbf{r})e^{-2(x-x_o)^2/\sigma_x'^2}e^{-2(y-y_o)^2/\sigma_y'^2}e^{-\gamma z}d^3\mathbf{r}$, where σ_x' and σ_y' are the probe-beam waists, (x_o, y_o) is the position of probe-beam center relative to the pump center and γ is the inverse penetration depth of the probe beam. A is the coefficient of carrier-induced reflectance (CCR), B is the coefficient of hot-electron thermoreflectance and C is the coefficient of phonon thermoreflectance. The carrier-induced reflectance originates from the dielectric response of free carriers introduced by the pump beam and the order of magnitude of CCR can be estimated using the Drude model (Sec. I within the Supplemental Material [33]).
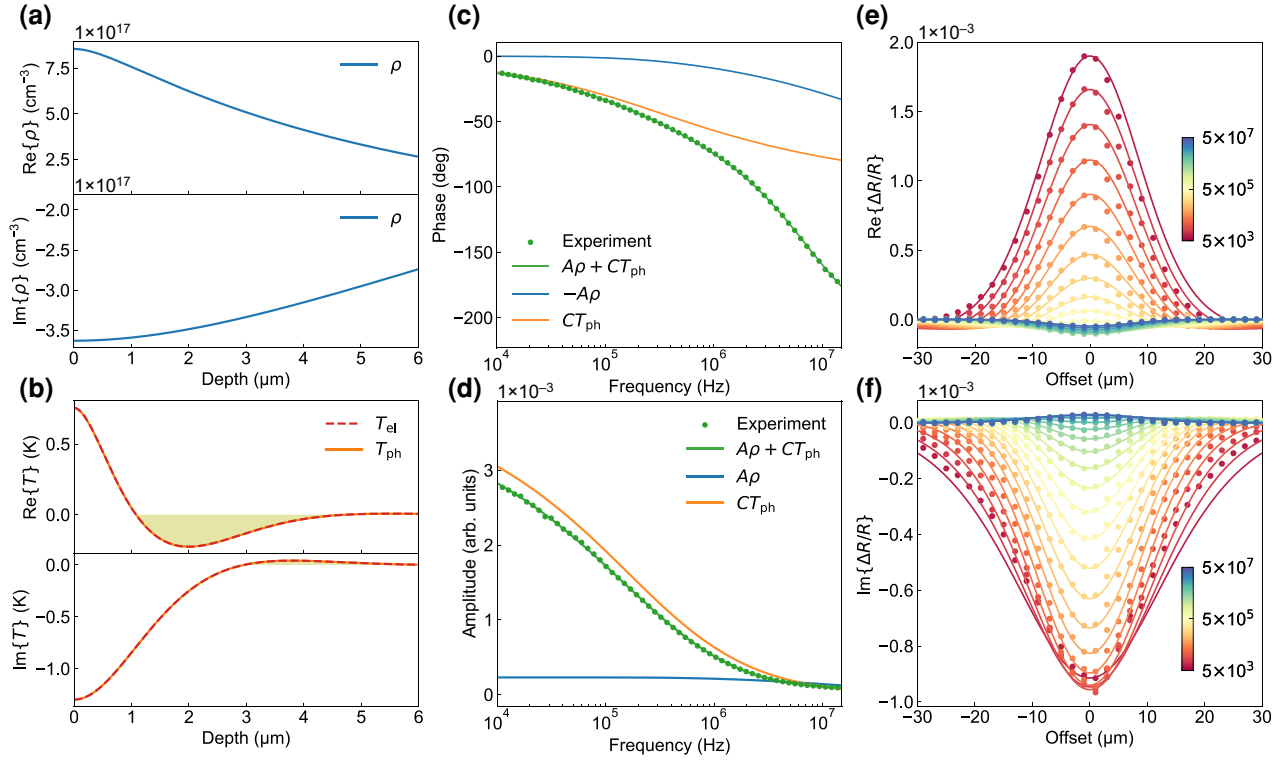
FIG. 2. (a) The excess carrier density profile $\overline{\rho}(z)$ and (b) the electron and phonon temperature distribution $\overline{T}_{\mathrm{el}}(z)$ and $\overline{T}_{\mathrm{ph}}(z)$ in p-type Si$_{0.98}$Ge$_{0.02}$ using the full model with modulation frequency $f = 7.96$ MHz and absorbed pump power $P_0 = 78$ mW at 273.15 K. The z-dependent carrier density and temperature profiles are obtained by $\overline{X}(z) = \frac{1}{\pi \sigma'_x \sigma'_y} \int X(\mathbf{r}) e^{-2x^2/\sigma'^2_x} e^{-2y^2/\sigma'^2_y} dx dy$. The weighted average of the carrier and temperatures can be computed by $\overline{X} = \gamma \int_0^\infty \overline{X}(z) e^{-\gamma z} dz$. The shaded area indicates the region where electron temperature has the opposite sign to the electron temperature at the surface. (c),(d) The phase and amplitude of photoreflectance $\frac{\Delta R}{R}$ in p-type Si$_{0.98}$Ge$_{0.02}$ at 273.15 K. The lines correspond to the best fits using the carrier and phonon model. Note in (c) we multiply the carrier part by negative one to plot the phases of different part of the signal together. (e),(f) The real and imaginary parts (Re $\left\{\frac{\Delta R}{R}\right\}$ and Im $\left\{\frac{\Delta R}{R}\right\}$) of the photoreflectance as a function of the beam offset distance, where the color represents the modulation frequency.

The electron and phonon thermoreflectance are caused by temperature-dependent electronic band structures and electron damping [34–37]. By examining Eqs. (2) and (3), we find that the electron and phonon temperature obey a simple relation, namely $\overline{T}_{\mathrm{el}} \approx \overline{T}_{\mathrm{ph}} \left(1 + \sqrt{i\omega/\omega_{\mathrm{e-p}}}\right)$, where the characteristic frequency for electron-phonon coupling $\omega_{\mathrm{e-p}} = g_{\mathrm{e-p}} \kappa_{\mathrm{el}} / C_{\mathrm{ph}} \kappa_{\mathrm{ph}}$ (Sec. VII.B within the Supplemental Material). This expression implies that the electron temperature has a smaller phase lag than the phonon temperature when the modulation frequency is much smaller than $\omega_{\mathrm{e-p}}$, as depicted in Fig. 1(d). In Ge, the characteristic frequency is found to be $\omega_{\mathrm{e-p}}/2\pi = 332$ MHz, where we take $C_{\mathrm{ph}} = 1.6 \times 10^6$ J/(m^3 K), $\kappa_{\mathrm{ph}} = 60$ W/(m K), $\kappa_{\mathrm{el}} = 2$ W/(m K) and $g_{\mathrm{e-p}} = 10^{17}$ W/(m^3 K) (according to Ref. [38], $g_{\mathrm{e-p}} \sim 10^{17} - 10^{18}$ W/(m^3 K) in GaAs, Si, AlAs, etc.). In the typical modulation frequency range in our experiment (500 Hz to 50 MHz), we make the approximation $\overline{T}_{\mathrm{el}} \approx \overline{T}_{\mathrm{ph}}$. We can therefore combine the electron and phonon temperatures' contributions in Eq. (4) into a single term $C\overline{T}_{\mathrm{ph}}$, where C can be regarded as the

effective coefficient of thermoreflectance (CTR). In this case, the photoreflectance signal consists of carrier and phonon contributions only. It can be shown that the phonon temperature can be calculated without the explicit knowledge of C_{el}, κ_{el}, and $g_{\mathrm{e-p}}$, as long as $\omega \ll \omega_{\mathrm{e-p}}$, which further simplifies the model (Sec. IV within the Supplemental Material [33]). We call such a simplified model the carrier and phonon model, in contrast to the model with the explicit inclusion of a distinct electron temperature and all relevant physical parameters, which we call the full model.

The average carrier density, electron, and phonon temperature under modulation are all represented by complex numbers, obtained from solving the transport equations, Eqs. (1), (2), and (3). Figure 2(a) illustrates that the real and imaginary part of the carrier density $\overline{\rho}(z)$ in Si$_{0.98}$Ge$_{0.02}$ decreases with depth as a consequence of ambipolar carrier diffusion. The unique feature of ambipolar diffusion under modulation is that it involves two types of diffusion lengths. In Si$_{0.98}$Ge$_{0.02}$, the ambipolar diffusivity is $D_a = 30.4$ cm^2/s and the carrier lifetime is

$\tau = 0.52$ μs at 273.15 K, yielding the ambipolar diffusion length $\sqrt{D_a \tau} = 39.8$ μm. However, at a modulation frequency $f = 7.96$ MHz, the decay length of the carrier density is much smaller than the ambipolar diffusion length, as it is also limited by the diffusion length over one period $\sqrt{D_a/(2\pi f)} = 7.8$ μm (Sec. II.A within the Supplemental Material [33]). The excited carrier density is on the order of 10^{17} cm^{-3}, much smaller than the typical excited carrier density by a pulsed laser (approximately 10^{19} cm^{-3}) [39]. This is because the carrier density's contribution to the photoreflectance under a pulsed pump laser becomes minimal once the delay time goes beyond the carrier recombination lifetime, whereas under a modulated cw pump there are constantly other carriers generated and the carrier-density part of the signal never decays with time, regardless of the modulation frequency. Our approach creates a nonequilibrium regime that is far more efficient in sensing carrier transport than pulsed-laser methods.

The phonon thermal diffusivity is given by $D_{ph} = \kappa_{ph}/C_{ph} = 0.29$ cm^2/s. Hence, the phonon diffusion length over one period (also known as the thermal penetration depth) is only $\sqrt{D_{ph}/(2\pi f)} = 0.76$ μm. Both the real and imaginary parts of phonon temperature decay with depth while oscillating across zero [Fig. 2(b)], as there is a spatially varying phase lag arising from the phonon diffusion (Sec. IX within the Supplemental Material [33]). The electron temperature has almost exactly the same distribution to the phonon temperature since $f \ll \omega_{e-p}/(2\pi)$, justifying our use of the simplified carrier and phonon model.

The transport coefficients used in Figs. 2(a) and 2(b) are obtained by fitting the experimental data with the carrier and phonon model. The fitting scheme is detailed in Sec. III. The photoreflectance is a complex number $\Delta R/R = re^{i\phi}$, where ϕ and r are the phase and amplitude. The phase and amplitude of the measured photoreflectance $\Delta R/R$ are presented in Figs. 2(c) and 2(d). Using the carrier and phonon model, we fit the phase and amplitude simultaneously to utilize the full information of the signal (Sec. III). We choose A, C, D_a, and κ_{ph} as fitting variables, as these variables have higher fitting sensitivities than others (see the sensitivity analysis in Sec. VI within the Supplemental Material [33]). We observe that the carrier and phonon model fits experimental data well. As the modulation frequency increases, the carrier transport plays a more and more significant role. At low modulation frequencies, the phase lag of the carrier density is zero and its amplitude approaches a constant.

The effective beam radius is a geometrical measure of carrier generation source, defined by $r_{eff} = \sqrt{(\sigma_{pump}^2 + \sigma_{probe}^2)/2}$, where σ_{pump} and σ_{probe} are the beam radii for the pump and probe beam. We find the effective beam radius is $r_{eff} = 10$ μm, by directly extracting it from a beam offset measurement at highest modulation

frequency. Since the effective beam radius is much smaller than the ambipolar diffusion length, the ambipolar diffusion reaches the steady-state limit $\overline{\rho}(\omega = 0) = P_0/(2\sqrt{\pi}E_{photon}D_a r_{eff})$ at low modulation frequencies $\omega \ll 4\pi^2 D_a/r_{eff}^2$ (Sec. II.A within the Supplemental Material [33]). In Si$_{0.98}$Ge$_{0.02}$, the phonon diffusion length is only slightly larger than the effective beam size at low modulation frequencies. With decreasing frequency, the phonon temperature has sufficient time to closely follow the modulated heating and rises to higher values, hence the amplitude of phonon temperature increases and the phase lag decreases. As a result, at low modulation frequencies, the phase is dominantly determined by the phonon temperature. As for the overall amplitude, it is dominated by the phonon temperature, yet the carrier part cannot be neglected. At high modulation frequencies, the phase lag of the carrier contribution starts to increase, since the diffusion length over one period $\sqrt{D_a/(2\pi f)}$ begins to limit the carrier distribution. Note that the carrier term $A\overline{\rho}$ and phonon term $C\overline{T}_{ph}$ contribute to the photoreflectance with the opposite signs. Consequently, the amplitude of photoreflectance is slightly lower than that of the phonon part above 50 MHz. The phase lag of the photoreflectance becomes much larger than that of phonon temperature. Eventually the phase lag surpasses 90°, which is the upper bound of temperature given by the Fourier heat-conduction model. This is a strong evidence that the reflectance signal cannot be explained by the phonon system alone.

We also study the case where the pump and probe beams are offset from one another. In Figs. 2(e) and 2(f), we show the real and imaginary parts of photoreflectance at various modulation frequencies when offsetting the pump with respect to the probe. At high modulation frequencies, the real and imaginary parts follow a Gaussian-like distribution with respect to the beam-offset distance. This is because the carrier and phonon diffusion are both smaller than the effective beam size and the geometry of excitation source plays a more significant role. At the modulation frequency decreases, both the carrier and phonon diffusion lengths increase, which is observed in the increase of the full width at half maximum of the real and imaginary components of the photoreflectance signals. We note that the real and imaginary components of the photoreflectance signals both experience a change of sign at certain modulation frequencies, which is not explainable by the Fourier heat-conduction model alone, but can be simply explained as a natural consequence of two contributions, the carrier-density term $A\overline{\rho}$ and phonon temperature term $C\overline{T}_{ph}$, respectively, having opposite signs. In other words, the CCR and CTR have opposite signs. The solid lines are solutions to the carrier and phonon model using the best fits without offset in Figs. 2(c) and 2(d). Although we did not directly fit the data with offset, the fact that the
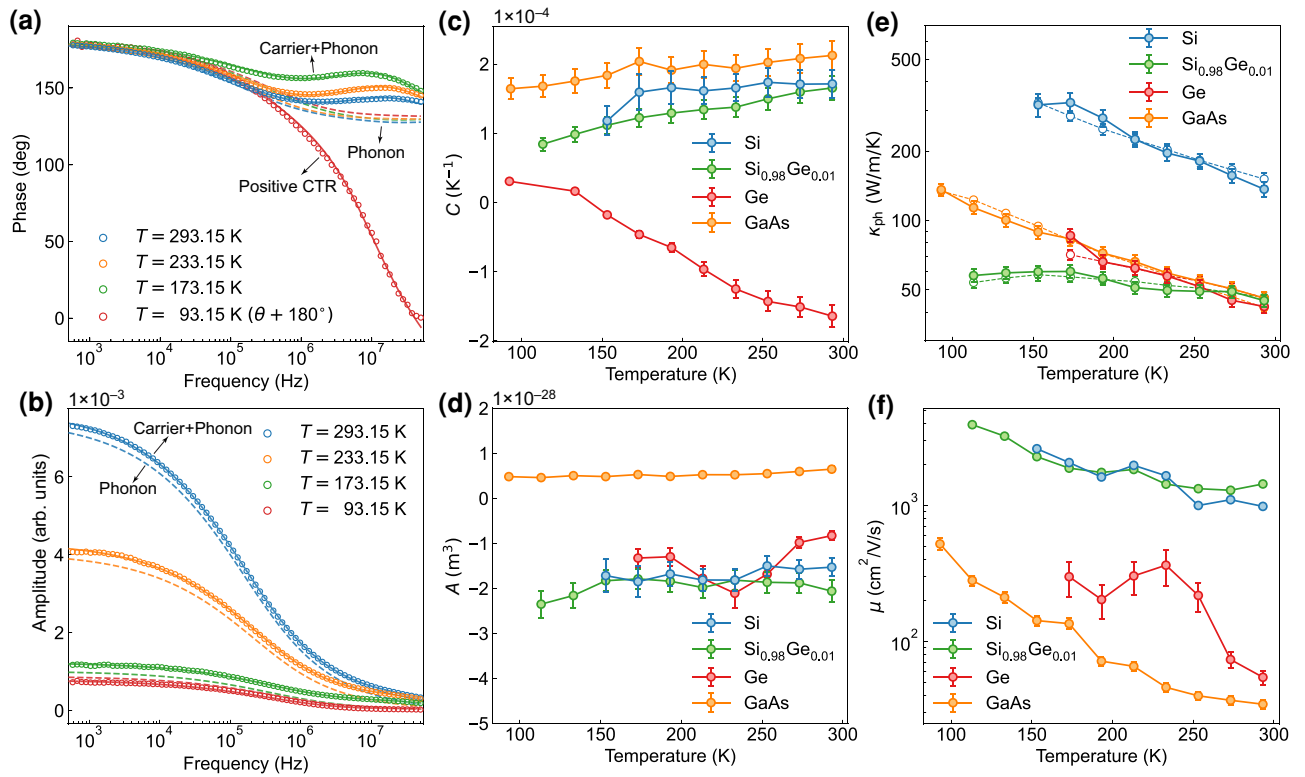
FIG. 3. Coefficients of reflectance and transport properties from temperature-dependent frequency-domain photoreflectance in several semiconductors. (a),(b) The phase and amplitude at different temperatures in p-type Ge. The solid lines are fitted values of $A\overline{\rho} + C\overline{T}_{ph}$ and the dashed lines are the phonon part $C\overline{T}_{ph}$. Note that at 93.15 K the phases of the photoreflectance and the phonon part are both shifted by 180° for comparative purposes with other temperatures, as the sign of CTR at 93.15 K is positive while negative at the other three temperatures. (c) The effective coefficients of thermoreflectance as a function of temperature. (d) The coefficients of carrier-induced reflectance as a function of temperature. (e) The phonon thermal conductivity from the direct measurement (filled circle) and a separate measurement with a metal transducer (open circle). (f) The ambipolar mobility as a function of temperature. The lifetime is assumed to be a temperature-independent constant as it mostly depends on the band gap and impurity concentrations and the lifetimes that give the best fits across all temperatures are 1.1 μs, 0.52 μs, 5 ns, 9 ns in Si, $Si_{0.98}Ge_{0.02}$, Ge, GaAs, respectively.

model and experiment match well with physically realistic parameters infers that the carrier and phonon model captures the essential physics correctly. The deviation between model and experiment at large offset distances and low modulation frequencies may be the result of a slightly asymmetric tilt in the incident pump beam with large offset as well as the impact $1/f$ noise.

We further validate our model by measuring several semiconductors at various temperatures. In Figs. 3(a) and 3(b), we show the phase and amplitude of photoreflectance in Ge. The signs of the CCR and CTR are the same at high temperatures. The total phase lag is smaller than that of the phonon temperature, as the carrier density generally has a low phase lag. At 93.15 K, the sign of the CTR flips and CCR and CTR now have opposite sign, hence we see that the amplitude of phonon part is larger than the total amplitude. The sign change of the CTR may be due to the competition between different interband electron transition channels as the band structure changes with temperature [34]. The sign flip in CTR

also significantly impacts the phase of photoreflectance. At the low temperature, the phase of photoreflectance curves downward with increasing frequency, when compared with phonon temperature. In contrast, the phase curves upward with frequency at higher temperatures due to the sign change in CTR (Fig. S8 within the Supplemental Material [33]) and eventually curves downward at even higher frequencies due to the shrinking carrier diffusion length over a period. In Si and $Si_{0.98}Ge_{0.02}$, the CCR is negative and the CTR is positive for the entire temperature range. In GaAs, both CCR and CTR are positive for the entire temperature range. According to the Drude model [40], the real part of refractive index n decreases with increasing carrier density ($dn/d\rho < 0$). Qualitatively speaking, the pump-induced free carriers can help to absorb more probe photons via free-carrier absorption [41], thus leading to a smaller reflectance. However, when the excited carriers are mostly localized near the surface in a length scale smaller than probe wavelength (e.g., trapped by defects), the electromagnetic field

of the probe photon inside the material is only partially altered [42]. Near the surface, $dn/d\rho$ contributes to the photoreflectance negatively (Sec. I.B within the Supplemental Material [33]). Consequently, the change in reflectance is positive, resulting in a positive CCR. The CTR generally has a much stronger temperature dependence than the CCR, because the temperature-dependent band structure and electron-phonon scattering rate both contribute to CTR, whereas though a temperature-dependent effective mass can cause change in CCR, it is a more subtle effect than the previously mentioned effects.

The phonon thermal conductivity in Si, $Si_{0.98}Ge_{0.02}$, Ge and GaAs from the frequency-domain photoreflectance agree well with the conventional FDTR measurements on gold-coated samples (the corresponding methodology can be found in Ref. [12]). The ambipolar mobility is given by $\mu = eD_a/k_BT$, where e is the elementary charge and the ambipolar mobility is related to the unipolar mobilities via $\mu = 2\mu_n\mu_p/(\mu_n + \mu_p)$, with μ_n and μ_p the electron and hole mobilities at their corresponding effective chemical potentials $E_{F,c}$ and $E_{F,v}$, respectively [43]. We find that the ambipolar mobility in Si and $Si_{0.98}Ge_{0.02}$ are similar while thermal conductivity in $Si_{0.98}Ge_{0.02}$ is much lower than that in Si, implying that the alloy scattering affects phonon transport more than carrier transport. GaAs has the lowest ambipolar mobility, as the low intrinsic hole mobility in GaAs significantly limits the ambipolar mobility despite the intrinsic high electron mobility. The mobility in Ge has a peak around 235 K. The peak can be partially due to the temperature-dependent electronic band structures and partially due to the uncertainty in fitting the ambipolar diffusion coefficient. As shown in Fig. 3(e), there is a peak in CCR around the same temperature as well, which signifies that CCR and ambipolar diffusivity can be inversely correlated in fitting.

To better understand the source of uncertainty in our fitting scheme, we conduct an uncertainty analysis. We first consider the case when $A/C = 10^{-24}$ m^3 K and $A/C = -10^{-24}$ m^3 K, with the remaining parameters taken from Ge's properties at 293.15 K. We then vary the pump beam radius and the ambipolar diffusion constant and calculate the corresponding uncertainty in D_a when fitting D_a and A together. The carrier lifetime in Ge is fixed at 5 ns, faster than most of the modulation periods. The carrier density at different $\mathbf{q}_\parallel$ is expressed by $\rho(\mathbf{q}_\parallel, z) \propto P_0/(D_a\sqrt{q_\parallel^2 + (D_a\tau)^{-1} + i\omega D_a^{-1}})$. As a result, the carrier part of the signal has a negligible imaginary part at most modulation frequencies. When the ambipolar diffusion length is significantly larger than the beam size, the carrier density approaches the steady-state limit, $\overline{\rho} \propto P_0/D_a$. When the ambipolar diffusion length is much smaller than the beam size, the carrier density is found to satisfy $\overline{\rho} \propto P_0/\sqrt{D_a}$ (Sec. II within the Supplemental Material [33]). In both cases, the mobility and the CCR are highly

anticorrelated, preventing us from fitting them together with very high confidence. When the ambipolar diffusion length is just slightly smaller than the beam size ($\sqrt{D_a\tau} \sim r_{eff}/2\pi$), the carrier density experiences both limits when sweeping the modulation frequency. This is advantageous since the change in the way that the signal depends on diffusivity (from one limit to the other limit) lowers the uncertainty. In Ge, the beam radius is much greater than the ambipolar diffusion length, corresponding to a region far below the zone of theoretical minimum uncertainty ($r_{eff} = 10$ µm, $\sqrt{D_a\tau} = 0.08$ µm in Ge at 293.15 K) in Fig. 4(a). Accordingly, we observe the enlarged uncertainty in Ge in Fig. 3(f). Other the other hand, if we flip the sign of the CCR, as illustrated in Fig. 4(b), the uncertainty is found to decrease. This is because the opposite signs of CCR and CTR lead to a larger phase lag than the phase lag of the phonon system alone. Consequently, in the same frequency-sweep range, the phase varies over a larger range thus leading to a higher sensitivity to and a lower uncertainty in the ambipolar diffusivity.

In $Si_{0.98}Ge_{0.02}$, the uncertainty is found to be much lower than Ge, for either case of $A/C > 0$ or $A/C < 0$. The carrier lifetime in $Si_{0.98}Ge_{0.02}$ is 0.52 µs, much larger than that in Ge. When the modulation frequency is on the same order of magnitude $\omega \sim \tau^{-1}$, the imaginary part in the carrier density becomes relevant. As we sweep the modulation frequency from low to high values, the carrier transport can be limited by the beam size, the diffusion length over one modulation period or the ambipolar diffusion length, depending on which quantity is the smallest. The carrier part of the signal is more sensitive to the diffusivity, which leads to a lower uncertainty than Ge. When $A/C > 0$, the real parts of the carrier-density term and the phonon temperature term are both positive and the phase lag of the signal is between the phase of the phonon temperature and the carrier density. When $A/C < 0$, the real parts of the carrier-density term and phonon-temperature term can cancel and the real part of the total signal can be either positive or negative. The narrow stripe with the lowest uncertainty corresponds to the near-zero real part at low modulation frequencies with a phase lag close to $90°$.

When the ambipolar diffusion length is above or below this stripe, the phase at low frequencies either approaches the phase of the phonon-temperature term ($0°$ when $\omega \rightarrow 0$) or the phase of the carrier-density term ($180°$ when $\omega \rightarrow 0$). As a consequence, near the stripe, the phase is highly sensitive to the carrier diffusivity. At large beam radius and large ambipolar diffusion length, the phonon part and carrier part of the signal may cancel (both the real and imaginary parts), leading to a near-zero total signal and hence increased uncertainty. On the other hand, when $A/C > 0$, a zero component in signal case will never occur for a finite modulation frequency.

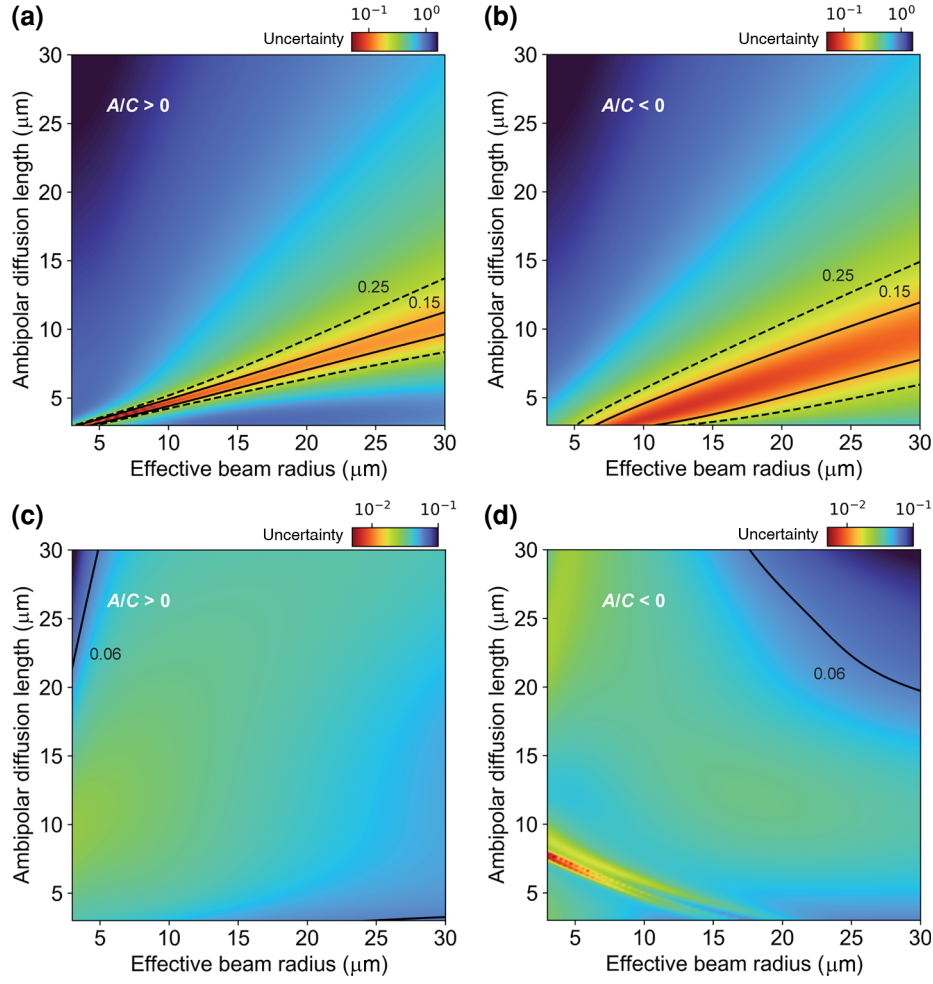To conclude, we model the carrier- and phonon-induced frequency-domain photoreflectance and explore

FIG. 4. The uncertainty of D_a when fitting D_a and A, as a function of the effective radius and the ambipolar diffusion length in Ge: (a) $A/C = 10^{24}$ m^3 K and (b) $A/C = -10^{24}$ m^3 K and in Si$_{0.98}$Ge$_{0.02}$: (c) $A/C = 10^{24}$ m^3 K and (d) $A/C = -10^{24}$ m^3 K. The color represents the common logarithm of the uncertainty. The uncertainty in the ambipolar diffusivity is lower in Si$_{0.98}$Ge$_{0.02}$ than Ge, since Si$_{0.98}$Ge$_{0.02}$ has a larger carrier lifetime. Note that to avoid the complexity from the choice of the scaling constant in front of the amplitude when fitting the phase and amplitude together, we consider the case of only fitting phase in this uncertainty analysis.

the possibility of applying the model to extract transport properties in semiconductors. In common semiconductors, the CCR is almost temperature independent and the CTR varies more with temperature. With the proper choice of modulation frequency and beam size, we can measure the ambipolar mobility, thermal conductivity, CCR and CTR at the same time with high confidence. Our modeling can be applied to analyze the transient reflectance as well, which expands the possibility of using optical reflectance to probe electron transport and phonon transport simultaneously.

III. METHODS

We use a fiber laser (Coherent OBIS LX 458 nm) with digital modulation of the power as the pump and a cw laser (Coherent OBIS LS 532 nm) as the probe. Little beam asymmetry along x and y directions for pump and probe are found therefore we assume pump and probe beam are both isotropic. The $1/e^2$ radius of the probe is $r_{probe} = 2.98\,\mu$m, determined by the knife-edge method (Fig. S18 within the Supplemental Material [33]). The effective beam radius can be extracted from the beam-offset measurement on a sample coated with gold thin film at the highest modulation frequency, as the amplitude at such a frequency is following a Gaussian distribution and the standard deviation is equal to $r_{eff}/\sqrt{2}$ (Fig. S19 within the Supplemental Material [33]). Then, the pump radius is $r_{pump} = \sqrt{2r_{eff}^2 - r_{probe}^2}$. The beam offset is achieved by moving the angle of the mirror to change the location of the pump beam while the probe beam is unchanged.

The probe beam goes through a half-wave plate first before reaching the sample. The half-wave plate is rotated by a motor until reaching an angle that minimizes the

intensity difference between the perturbed (reflected off the sample) and unperturbed probe so that their common noises are reduced. Then, the unperturbed probe and perturbed probe are sent to a balanced photodetector. The detected signal is amplified by the lock-in amplifier (Zurich Instruments HF2LI). We take the ratio of the ac part divided by the dc part as the photoreflectance signal. Note that we measure the pump phase before measuring the sample and make sure it is subtracted in the measured phase. We also make sure the perturbed and unperturbed probe beam do not have any optical path difference as it can lead to a larger phase difference at higher modulation frequencies. Other details of the setup can be found in Refs. [44,45].

The Si, Si$_{0.98}$Ge$_{0.02}$, Ge and GaAs are commercial available (MTI Corp.) with resistivity $1 - 10$ Ω cm, > 50 Ω cm, $0.0007 - 0.005$ Ω cm, $0.6 \times 10^8 - 2.0 \times 10^8$ Ω cm, respectively. For measurements with a transducer, the gold thin film is coated using an E-beam evaporator. A 3-nm Ti layer is used as the adhesion layer and another 92-nm Au layer is deposited, confirmed by the SEM image.

We use a nonlinear least-squares fitting scheme to extract material properties of interest. We vectorize the amplitude and phase data at N modulation frequency points into a $2N$-by-1 vector $\mathbf{v} = (r_1, r_2, \ldots, r_N, \phi_1, \phi_2, \ldots, \phi_N)^{\mathrm{T}}$. Since the amplitude (dimensionless) and the phase (in the unit of degrees) are typically at different orders of magnitude, we rescale the amplitudes r_i by a scaling factor of 10^4. The objective function is defined by the difference between the measured and the computed data, $\mathbf{f}(\mathbf{x}) = \mathbf{v}_{\text{expt.}} - \mathbf{v}_{\text{model}}(\mathbf{x})$, where $\mathbf{x} = (x_1, x_2, \ldots, x_M)^{\mathrm{T}}$ is the vector consisting of M variables to be fitted. The goal of the optimization is to find the best fits of $\mathbf{x}$ that minimize the L^2 norm of the objective function $\|\mathbf{f}(\mathbf{x})\|$. We use the lsqnonlin function in MATLAB to perform this optimization.

The experimental data and the modeling data from the best fits for phase and amplitude for all samples can be found in Sec. VIII within the Supplemental Material [33]. The error bar in the transport properties for the sample with gold transducer are calculated using the Monte Carlo method. The parameters in the Fourier heat-conduction model, except the fitting variables, are randomly sampled in 100 times according to the normal distribution with an assumed relative standard deviation of 3%. The fitted variables roughly follow normal distributions with different standard deviations. The error bar in Fig. 3 and the uncertainty in Fig. 4 are both computed using the covariance matrix assuming a 3% uncertainty in all parameters except the fitting variables. The formalism to compute the covariance matrix is detailed in Ref. [46]. We also briefly discuss how to model non-Fourier phonon heat conduction in Sec. X within the Supplemental Material [33] following Ref. [47].

[1] D. Burg and J. H. Ausubel, Moore's Law revisited through Intel chip density, PLOS One **16**, e0256245 (2021).

[2] W. Cao, H. Bu, M. Vinet, M. Cao, S. Takagi, S. Hwang, T. Ghani, and K. Banerjee, The future transistors, Nature **620,** 501 (2023).

[3] E. Pop, S. Sinha, and K. E. Goodson, Heat generation and transport in nanometer-scale transistors, Proc. IEEE **94,** 1587 (2006).

[4] M. S. Lundstrom and M. A. Alam, Moore's law: The journey ahead, Science **378,** 722 (2022).

[5] R. G. Kepler, Charge carrier production and mobility in anthracene crystals, Phys. Rev. **119,** 1226 (1960).

[6] F. J. Morin and J. P. Maita, Electrical properties of silicon containing arsenic and boron, Phys. Rev. **96,** 28 (1954).

[7] D. G. Cahill, Thermal conductivity measurement from 30 to 750 K: The 3ω method, Rev. Sci. Instrum. **61,** 802 (1990).

[8] C. A. Paddock and G. L. Eesley, Transient thermoreflectance from thin metal films, J. Appl. Phys. **60,** 285 (1986).

[9] W. S. Capinski and H. J. Maris, Improved apparatus for picosecond pump-and-probe optical measurements, Rev. Sci. Instrum. **67,** 2720 (1996).

[10] D. G. Cahill, Analysis of heat flow in layered structures for time-domain thermoreflectance, Rev. Sci. Instrum. **75,** 5119 (2004).

[11] A. Rosencwaig, J. Opsal, W. L. Smith, and D. Willenborg, Detection of thermal waves through optical reflectance, Appl. Phys. Lett. **46,** 1013 (1985).

[12] A. J. Schmidt, R. Cheaito, and M. Chiesa, A frequency-domain thermoreflectance method for the characterization of thermal properties, Rev. Sci. Instrum. **80,** 094901 (2009).

[13] T. Tanaka, A. Harata, and T. Sawada, Subpicosecond surface-restricted carrier and thermal dynamics by transient reflectivity measurements, J. Appl. Phys. **82,** 4033 (1997).

[14] A. L. Smirl, S. C. Moss, and J. R. Lindle, Picosecond dynamics of high-density laser-induced transient plasma gratings in germanium, Phys. Rev. B **25,** 2645 (1982).

[15] U. Choudhry, T. Kim, M. Adams, J. Ranasinghe, R. Yang, and B. Liao, Characterizing microscale energy transport in materials with transient grating spectroscopy, J. Appl. Phys. **130,** 231101 (2021).

[16] J. A. Johnson, A. A. Maznev, J. Cuffe, J. K. Eliason, A. J. Minnich, T. Kehoe, C. M. S. Torres, G. Chen, and K. A. Nelson, Direct measurement of room-temperature nondiffusive thermal transport over micron distances in a silicon membrane, Phys. Rev. Lett. **110,** 025901 (2013).

[17] J. Shin, G. A. Gamage, Z. Ding, K. Chen, F. Tian, X. Qian, J. Zhou, H. Lee, J. Zhou, L. Shi, Thanh Nguyen, Fei Han, Mingda Li, David Broido, Aaron Schmidt, Zhifeng Ren, and Gang Chen, High ambipolar mobility in cubic boron arsenide, Science **377,** 437 (2022).

[18] L. Wang, R. Cheaito, J. Braun, A. Giri, and P. Hopkins, Thermal conductivity measurements of non-metals via combined time-and frequency-domain thermoreflectance without a metal film transducer, Rev. Sci. Instrum. **87,** 094902 (2016).

[19] S. Warkander and J. Wu, Transducerless time domain reflectance measurement of semiconductor thermal properties, J. Appl. Phys. **131,** 025101 (2022).

[20] L. Waldecker, R. Bertoni, R. Ernstorfer, and J. Vorberger, Electron-phonon coupling and energy flow in a simple metal beyond the two-temperature approximation, Phys. Rev. X **6,** 021003 (2016).

[21] R. B. Wilson and S. Coh, Parametric dependence of hot electron relaxation timescales on electron-electron and electron-phonon interaction strengths, Commun. Phys. **3,** 179 (2020).

[22] X. Qian, Z. Ding, J. Shin, A. J. Schmidt, and G. Chen, Accurate measurement of in-plane thermal conductivity of layered materials without metal film transducer using frequency domain thermoreflectance, Rev. Sci. Instrum. **91,** 064903 (2020).

[23] J. Zhang, E. M. Levenson-Falk, B. Ramshaw, D. Bonn, R. Liang, W. Hardy, S. A. Hartnoll, and A. Kapitulnik, Anomalous thermal diffusivity in underdoped YBa$_2$Cu$_3$O$_{6+x}$, Proc. Natl. Acad. Sci. **114,** 5378 (2017).

[24] J. Opsal, M. W. Taylor, W. L. Smith, and A. Rosencwaig, Temporal behavior of modulated optical reflectance in silicon, J. Appl. Phys. **61,** 240 (1987).

[25] J. R. Goldman and J. A. Prybyla, Ultrafast dynamics of laser-excited electron distributions in silicon, Phys. Rev. Lett. **72,** 1364 (1994).

[26] J. F. Young and H. M. van Driel, Ambipolar diffusion of high-density electrons and holes in Ge, Si, and GaAs: Many-body effects, Phys. Rev. B **26,** 2147 (1982).

[27] C.-M. Li, T. Sjodin, and H.-L. Dai, Photoexcited carrier diffusion near a Si(111) surface: Non-negligible consequence of carrier-carrier scattering, Phys. Rev. B **56,** 15252 (1997).

[28] J. Sjakste, N. Vast, G. Barbarino, M. Calandra, F. Mauri, J. Kanasaki, H. Tanimura, and K. Tanimura, Energy relaxation mechanism of hot-electron ensembles in GaAs: Theoretical and experimental study of its temperature dependence, Phys. Rev. B **97,** 064302 (2018).

[29] H. M. van Driel, Influence of hot phonons on energy relaxation of high-density carriers in germanium, Phys. Rev. B **19,** 5928 (1979).

[30] S. Sarkar, I.-W. Un, Y. Sivan, and Y. Dubi, Theory of non-equilibrium 'hot' carriers in direct band-gap semiconductors under continuous illumination, New J. Phys. **24,** 053008 (2022).

[31] C. J. Glassbrenner and G. A. Slack, Thermal conductivity of silicon and germanium from 3°K to the melting point, Phys. Rev. **134,** A1058 (1964).

[32] D. K. Schroder, *Semiconductor Material and Device Characterization* (John Wiley & Sons, Inc., Hoboken, New Jersey, 2015).

[33] See Supplemental Material at http://link.aps.org/supplemental/10.1103/PhysRevApplied.21.034044 for derivations of equations, details of the modeling, and raw data.

[34] E. Matatagui, A. G. Thompson, and M. Cardona, Thermoreflectance in semiconductors, Phys. Rev. **176,** 950 (1968).

[35] D. J. Chadi and R. M. White, Frequency- and wave-number-dependent dielectric function of semiconductors, Phys. Rev. B **11,** 5077 (1975).

[36] K. Liu, X. Shi, F. Angeles, R. Mohan, J. Gorchon, S. Coh, and R. B. Wilson, Differentiating contributions of electrons and phonons to the thermoreflectance spectra of gold, Phys. Rev. Mater. **5,** 106001 (2021).

[37] A. Block, R. Yu, I.-W. Un, S. Varghese, M. Liebel, N. F. van Hulst, S. Fan, K.-J. Tielrooij, and Y. Sivan, Observation of negative effective thermal diffusion in gold films, ACS Photonics **10,** 1150 (2023).

[38] S. Sadasivam, M. K. Y. Chan, and P. Darancet, Theory of thermal relaxation of electrons in semiconductors, Phys. Rev. Lett. **119,** 136602 (2017).

[39] J. Zhou, H. D. Shin, K. Chen, B. Song, R. A. Duncan, Q. Xu, A. A. Maznev, K. A. Nelson, and G. Chen, Direct observation of large electron–phonon interaction effect on phonon heat transport, Nat. Commun. **11,** 6040 (2020).

[40] L.-A. Lompré, J.-M. Liu, H. Kurz, and N. Bloembergen, Optical heating of electron-hole plasma in silicon by picosecond pulses, Appl. Phys. Lett. **44,** 3 (1984).

[41] X. Zhang, G. Shi, J. A. Leveillee, F. Giustino, and E. Kioupakis, *Ab initio* theory of free-carrier absorption in semiconductors, Phys. Rev. B **106,** 205203 (2022).

[42] D. Aspnes and A. Frova, Influence of spatially dependent perturbations on modulated reflectance and absorption of solids, Solid State Commun. **7,** 155 (1969).

[43] M. Beck, D. Streb, M. Vitzethum, P. Kiesel, S. Malzer, C. Metzner, and G. H. Döhler, Ambipolar drift of spatially separated electrons and holes, Phys. Rev. B **64,** 085307 (2001).

[44] J. Yang, C. Maragliano, and A. J. Schmidt, Thermal property microscopy with frequency domain thermoreflectance, Rev. Sci. Instrum. **84,** 104904 (2013).

[45] J. Yang, E. Ziade, and A. J. Schmidt, Modeling optical absorption for thermoreflectance measurements, J. Appl. Phys. **119,** 095107 (2016).

[46] J. Yang, E. Ziade, and A. J. Schmidt, Uncertainty analysis of thermoreflectance measurements, Rev. Sci. Instrum. **87,** 014901 (2016).

[47] V. Chiloyan, S. Huberman, Z. Ding, J. Mendoza, A. A. Maznev, K. A. Nelson, and G. Chen, Green's functions of the Boltzmann transport equation with the full scattering matrix for phonon nanoscale transport beyond the relaxation-time approximation, Phys. Rev. B **104,** 245424 (2021).